RESEARCH ARTICLE
SOLID EARTH: SEISMOLOGY

Earth and Planetary Physics
4: 1–12, 2020
doi: 10.26464/epp2020067

Sharpness of the paired 660-km discontinuity beneath the Izu-Bonin area

LiMing Wang[1], and XiaoBo He[2*]

[1]Department of Marine Sciences, Zhejiang University, Zhoushan Zhejiang 316021, China;

[2]Marine Acoustics and Remote Sensing Laboratory, Zhejiang Ocean University, Zhoushan Zhejiang 316022, China

Key Points:

- The 660-km discontinuity appears to be paired at depths of 660 and 720 km in Izu–Bonin
- The sharpness of the 660-km discontinuity is ~5 km, whereas that of the 720-km discontinuity is ~20 km
- The upper discontinuity is due to post-spinel transition, whereas the lower discontinuity is likely due to a phase transition from majoritic garnet to perovskite in mid-oceanic ridge basalt

Citation: Wang, L. M. and He, X. B. (2020). Sharpness of the paired 660-km discontinuity beneath the Izu-Bonin area. *Earth Planet. Phys.*, *4*(6), 1–12. http://doi.org/10.26464/epp2020067

Abstract: The 660-km discontinuity that separates the Earth's upper and lower mantle has primarily been attributed to phase changes in olivine and other minerals. Resolving the sharpness is essential for predicting the composition of the mantle and for understanding its dynamic effects. In this study, we used S-to-P conversions from the 660-km interface, termed S660P, arriving in the P-wave coda from one earthquake in the Izu–Bonin subduction zone recorded by stations in Alaska. The S660P signals were of high quality, providing us an unprecedented opportunity to resolve the sharpness of the discontinuity. Our study demonstrated, based on the impedance contrast given by the IASP91 model, that the discontinuity has a transitional thickness of ~5 km. In addition, we observed a prominent arrival right after the S660P, which was best explained by S-to-P conversions from a deeper discontinuity at a depth of ~720 km with a transitional thickness of ~20 km, termed S720P. The 720-km discontinuity is most likely the result of a phase transition from majoritic garnet to perovskite in the segregated oceanic crust (mainly the mid-oceanic ridge basalt composition) at the uppermost lower mantle beneath this area. The inferred phase changes are also consistent with predictions from mineral physics experiments.

Keywords: 660-km discontinuity; S-to-P conversions; Izu–Bonin; sharpness; mid-oceanic ridge basalt

1. Introduction

The seismic discontinuity in the mantle at an average depth of 660 km that results from the transformation of ringwoodite (γ-spinel) into perovskite and magnesiowüstite (Ringwood, 1975) has been observed globally, leading to the conclusion that it is a first-order discontinuity (Shearer, 2000). A subducting slab may penetrate or stagnate at the 660-km discontinuity (e.g., Fukao and Obayashi, 2013), and hot upwellings may also deflect at this boundary (French and Romanowicz, 2015). Hence, the 660-km discontinuity is thought to be an important boundary in the mantle, especially with respect to mantle dynamics. Most previous seismological studies have focused on constraining the varying depths of this discontinuity to measure the thickness of the transition zone (e.g., Shearer and Masters, 1992; Lawrence and Shearer, 2006). The sharpness of this discontinuity, however, remains open to debate.

Early receiver function studies revealed that the transition thickness of the 660-km discontinuity could be up to 20–30 km (Petersen et al., 1993). In addition, analyses of precursors to PKPPKP have shown that the transition thickness is 4 km or less, and S-to-P conversions have suggested that the thickness is at most 5 km (Yamazaki and Hirahara, 1994). However, in another study of S-to-P conversions, Tibi and Wiens (2005) concluded that the transition zone is less than 2 km thick. A subsequent study of the receiver function indicated that it is ~11.5 km thick (Lawrence and Shearer, 2006). A previous study of S-to-P converted waves (Castle and Creager, 2000) and a recent study on triplicated waves (Zhang M et al., 2019) both suggested that the 660-km discontinuity is sharp (<10 km). However, other triplication studies have suggested the existence of a broad (~50 to 70 km thick) 660-km discontinuity (e.g., Wang BS and Niu FL, 2010; Li J et al., 2013). Therefore, the seismological constraints on the sharpness of the transition zone still remain inconclusive.

In addition, multiple seismic discontinuities near the base of the transition zone have typically been seen in thermally anomalous areas (e.g., Simmons and Gurrola, 2000; Deuss et al., 2006; Schultz and Gu YJ, 2013), particularly in subduction zones (e.g., Tibi et al., 2007; Zhou YZ et al., 2012), yet the causes of multiplication are not fully understood. Nonolivine components have often been in-

Correspondence to: X. B. He, xbhe@zju.edu.cn
Received 31 JAN 2020; Accepted 27 JUL 2020.
Accepted article online .

voked to explain this phenomenon (e.g., Vacher et al., 1998). Previous observations have primarily relied on stacked energy, such as receiver function imaging and slant-stacked S-to-P vespagrams; hence, waveform modeling is urgently needed to further understand the mantle discontinuities, especially beneath subduction zones. In this study, we observed S-to-P converted waves from one event in the Izu–Bonin subduction zone recorded by stations in Alaska to investigate the mantle structure near a 660-km depth and to find evidence for two seismic discontinuities in this area.

2. Data and Analyses

The seismic data used in this study were recorded by the regional seismic network in Alaska (Figure 1), which consists of 27 broadband seismic stations. We used seismograms of one deep-focus earthquake (M_w 6.1) that occurred on April 21, 2013, at a depth of 422 km in the Izu–Bonin subduction zone (Figure 1). A vertical cross section along a profile defined by the source and stations containing the P-wave velocity perturbations given by Fukao and Obayashi (2013) and S-to-P ray paths is presented in Figure 2.

We applied a two-pass, two-pole Butterworth bandpass filter with corner frequencies at 0.05 and 0.5 Hz to the records of the vertical component. We analyzed the S-to-P converted wave (SdP), which is a seismic phase that descends as an S wave from the earthquake source and then converts to a P wave at the deep velocity interfaces (e.g., Zhou YZ et al., 2012; Li J and Yuen, 2014; Niu FL, 2014; Yang ZT and He XB, 2015; Cui QH et al., 2018; He XB and Zheng YX, 2018). Hence, SdP exhibits a nearly identical (slightly lower) slowness compared with direct P, which helps identify them in the vespagram calculated by an *N*th (N = 4) root slant-stack algorithm (e.g., Rost and Thomas, 2002; Hu JF and He XB, 2019). One-dimensional waveform modeling based on a propagation matrix algorithm (Wang RJ, 1999) was also conducted to further understand the nature of the mantle discontinuities. The Global Centroid Moment Tensor (CMT) solution was used for the source mechanism. The source time function was constructed as normalized square half-sinusoid.

All the velocity seismograms were aligned along the direct P wave and plotted as a function of the epicentral distance (Figure 3a). The record section shows two remarkably prominent arrivals at ~20–26 s after the direct P wave. The first arrival was identified as the S-to-P conversion at the 660-km discontinuity, whereas the second was not predicted by the IASP91 model (Kennett and Engdahl, 1991). The double arrivals were also clear on the vespagram (Figure 3c). Note that the IASP91 model largely explained the S660P in terms of its amplitude and slowness. Thus, we modified the IASP91 model only slightly to reproduce the S660P behavior. We also conducted frequency–wavenumber analyses (Figure 4) showing that the directions of the arrivals were along the great-circle ray path, which indicated that off-azimuth wave propagation was not needed in the modeling (Rost and Thomas, 2002). The record sections comprising the velocity seismograms rotated to the LQT coordinate system are presented in Figure 5 and show a large amplitude in the *L* component and weak signals in the *Q* and *T* components. This behavior further validated that the later

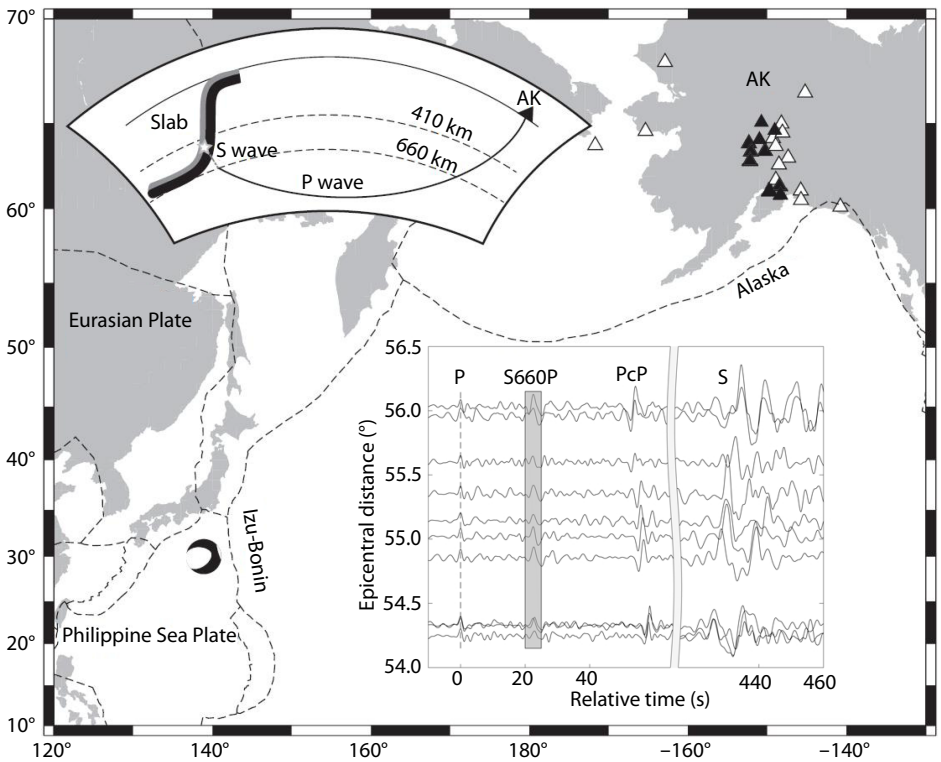

Figure 1. Locations of the single earthquake event (beach ball) that occurred on April 21, 2013, and the 27 seismic stations (triangles) located in Alaska. The upper-left inset is a schematic plot depicting the ray path that an S-to-P converted wave takes through the Earth. The bottom-right inset presents the traces recorded by 10 stations (solid triangles) used in this study, and the gray-shaded region highlights the S660P signals arriving in the P-coda.

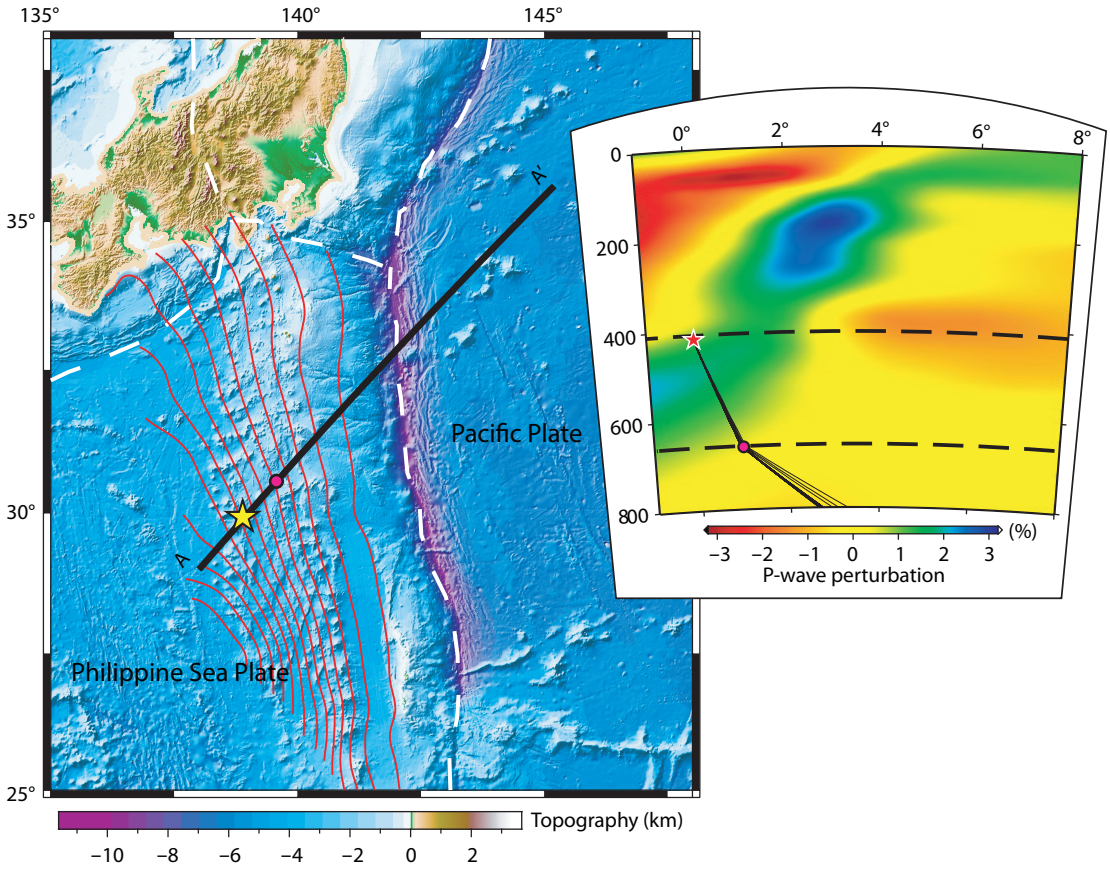

Figure 2. Left: a map showing tectonic settings of the study region. The red lines denote the depth contours of the upper boundaries of the subducting Pacific slab. The event and S-to-P conversion point at 660-km depth are denoted as star and circle, respectively. Right: a vertical cross-section showing the P-wave velocity perturbations along A-A′ profile given by the model of Fukao and Obayashi (2013), and the black lines denote the S-to-P ray paths at source-side calculated via the TauP toolkit (Crotwell et al., 1999) based on the IASP91 model (Kennett and Engdahl, 1991).

arrivals after P were S-to-P converted waves. The distribution of S-to-P piercing points at the 660-km discontinuity was calculated by using the TauP toolkit (Crotwell et al., 1999) according to the IASP91 model. These results are presented in Figure 6.

3. Results and Discussion

The vespagram of the record section comprising the velocity seismograms is shown in Figure 3c, whereas that of the synthetic section is shown in Figure 3d. The later arrival after P exhibits a negative relative slowness of ~0.1 s/degree with respect to the P wave, suggesting that it is likely an S-to-P converted wave from a mantle discontinuity below the source. This arrival was also predicted by the IASP91 model, leading to the conclusion that this later arrival was more likely a product of S-to-P conversion occurring at a depth of 660 km. Before we used the S660P-P differential travel times to refine the conversion depth, we first used the pP-P differential travel times to reconstrain the focal depth (Figure 7a). This step yielded a depth of 428 km, which best fit the data. We further obtained a more precise conversion depth of ~657 km, which best explained the observed differential travel times of S660P-P (Figure 7b). The slight elevation of depth by 3 km with respect to the 660-km depth could have been caused by a high-temperature anomaly of ~55 K according to the negative Clapeyron slope (−2.8 MPa/K) of the transition of ringwoodite to perovskite and magnesiowüstite given by Ito and Takahashi (1989). However, such a small perturbation is more likely less than the uncertainty of constraints of the 660-km discontinuity caused by a number of factors, such as the three-dimensional heterogeneity and source location. Therefore, we focused primarily on the sharpness of this discontinuity and not on the depth.

3.1 Sharpness of the 660-km Discontinuity

As shown in the inset of Figure 1, the later arrivals were characterized by a high signal-to-noise ratio, which allowed us to place tight constraints on the sharpness of the phase transition at the 660-km depth. We used data with better quality (more specifically, data that showed clear onset and coherent wave arrivals) from 10 stations for the analyses. Detailed information on the 10 stations is listed in Table 1. We used the amplitude (peak-to-peak) ratio of S660P versus S to constrain the phase transition sharpness at the 660-km depth. Note that the use of paired phases could significantly minimize the effects of the source radiation pattern and scattering along the ray paths. A series of models were constructed to compare with the observed amplitude ratios by varying the transitional thickness of the S-to-P conversion at the 660-km depth from 0 to 15 km in increments of 1 km. The impedance con-

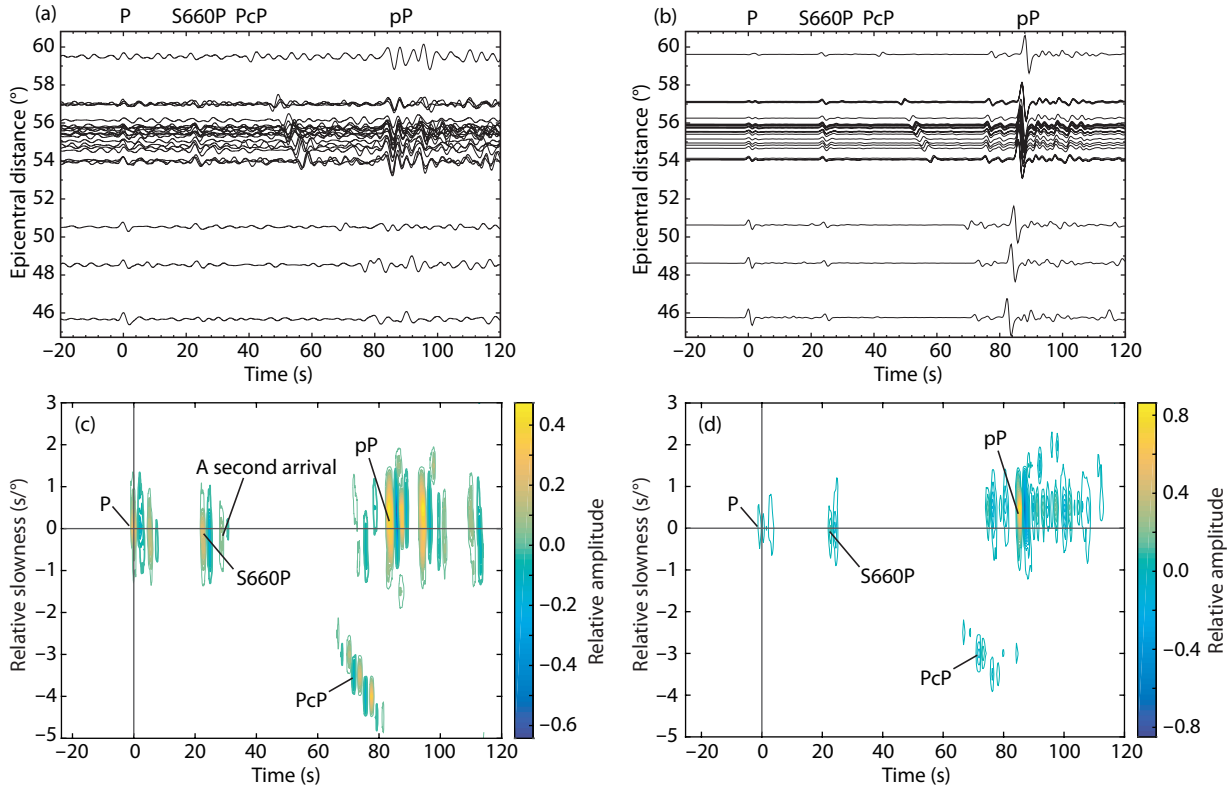

Figure 3. (a, c) The record section comprising velocity seismograms along with the fourth root vespagram of the data. (b, d) The synthetic section based on the IASP91 model (Kennett and Engdahl, 1991) along with the fourth root vespagram of the synthetics. Four prominent seismic phases (P, S660P, PcP, and pP) are named. Note that the S660P is predicted by the IASP91 model, but the arrival after S660P is not predicted, indicating a particular structure is needed to explain this arrival. Additionally, a cluster of energy occurring around 95 s is observable, which may be a product of reverberations within a water layer or a shallow structure below pP bounce points at the surface (e.g., Huang JP et al., 2015).

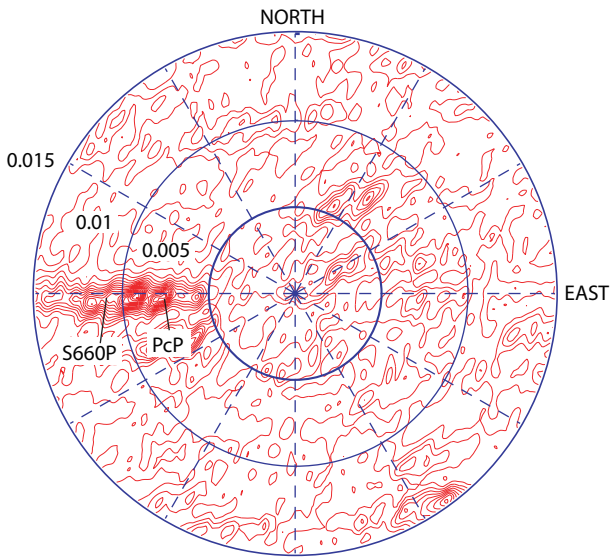

Figure 4. The F-K diagram calculated for S660P and PcP phases, showing their signals come from the same direction defined by the source and array.

trast and compressional wave velocity/shear wave velocity (V_P/V_S) ratio were the same as those of the IASP91 model.

The thickness of the transition for the 660-km discontinuity was finally determined to be ~5 km with a standard deviation of 4 km, which best fit the data (Figure 8a). The great similarity in waveforms between the data and the synthetics suggests that the preferred model replicated the observations well (Figure 8b). The sharp 660-km discontinuity seen in this study is consistent with an early work by Castle and Creager (2000) and a recent work by Zhang M et al. (2019), which suggest that the discontinuity is at most 10 km thick, and it is marginally consistent with a previous S-to-P conversion study that concluded the discontinuity is ≤5 km thick (Yamazaki and Hirahara, 1994). A sharp 660-km discontinuity resulting from the post-spinel transition was also revealed in a recent mineral physics experiment by Ishii et al. (2019). The broadened 660-km discontinuity observed before (e.g., Wang BS and Niu FL, 2010; Li J et al., 2013) was explained by the multiple phase transitions associated with dissolution of the olivine and garnet components (Wang BS and Niu FL, 2010), whereas the sharp 660-km discontinuity observed in this study referred only to the phase change of the olivine component.

Note that the derived transition thickness clearly depends on the impedance contrast across the 660-km discontinuity because a tradeoff exists between the sharpness and the impedance contrast, which was given by the IASP91 model in this study. The impedance contrasts across this discontinuity in the IASP91 and

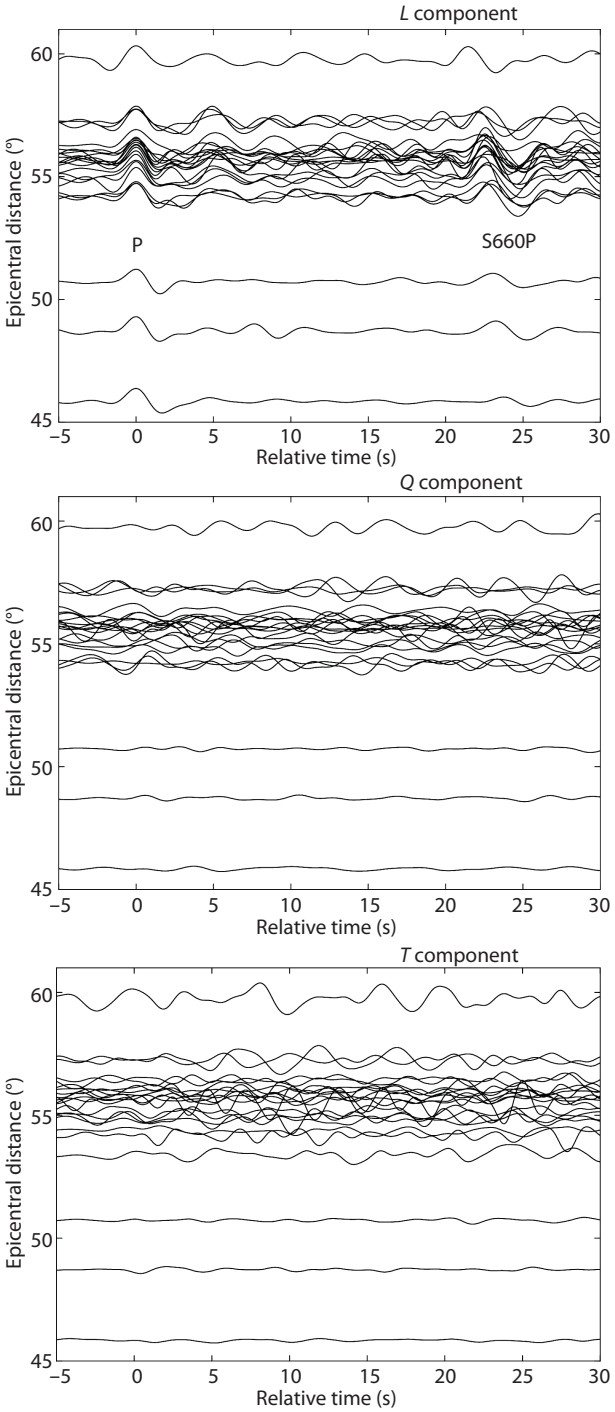

Figure 5. The record-sections in the LQT coordinate system.

PREM (Dziewonski and Anderson, 1981; isotropic version) models were very similar, leading to a very great similarity in synthetic S660P waveforms based on the two models. A comparison is presented in Figure 9.

To examine whether the source radiation pattern affected the constrained sharpness, we selected traces from four stations (Figure 10) and used an amplitude ratio of S660P versus PcP to constrain the sharpness. Compared with the PcP phase, the recorded direct P wave was weaker; thus, we used the amplitude ratio of S660P versus PcP for the analyses. Data recorded by the four

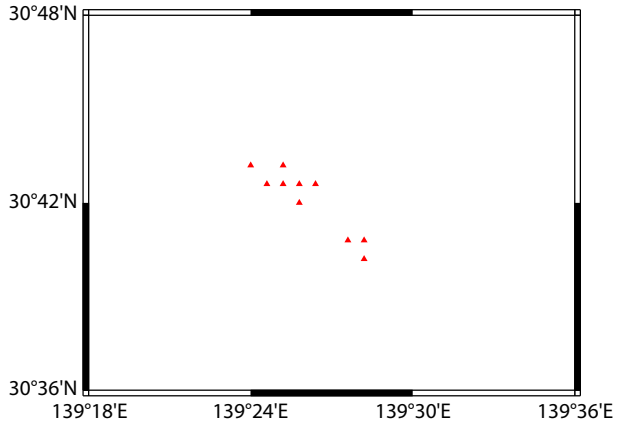

Figure 6. The distribution of 10 S660P piercing points at the 660 km depth corresponding to the 10 seismograms presented in Figure 1, which are selected because of their high quality.

stations (BPAK, NEA, MLY, and PPLA) that exhibited a better quality were used. Detailed information on the four stations is presented in Table 2. Our analyses yielded a transition thickness of ~5 km (Figure 11), which agreed well with the constrained result when using the amplitude ratio of S660P versus S (Figure 8), suggesting that the result was independent of the source radiation pattern. The nature of this sharp transition also helped rule out the contribution of the nonolivine component (e.g., majorite garnet to bridgmanite) to the 660-km discontinuity, which occurs at ~660-km depth but over a broad interval of ~35 km or more (e.g., Vitos et al., 2006). We then used the arrival after S660P to characterize the deeper mantle discontinuity.

3.2 Origin of the 720-km Discontinuity

Our last goal was to understand the origin of the later arrival after S660P. We concluded, based on its slowness and arrival time, that it was also a product of the S-to-P conversion but occurred at a greater depth. We constructed a series of models with various conversion depths and velocity changes to fit the observed waveform by a straightforward approach of trial and error (Figure 12). Specifically, we first searched for the proper depth to explain its arrival time, and then adjusted the impedance contrast across the discontinuity to fit the amplitude. We also slightly modified the resolved depth again to better explain both the arrival time and amplitude. Our final preferred model demonstrated that the conversion begins at a 725-km depth and ends at a 745-km depth and that the V_S, V_P, and density increase by 4.5%, 4.3%, and 3.2%, respectively, over a width of 20 km, which best explains the observations.

Nonolivine mantle components in a pyrolytic mantle (peridotite) have often been invoked to explain the multiple discontinuities (e.g., Ai YS et al., 2003). However, the fact is that the majoritic garnet–bridgmanite in the coexisting field is relatively broad (~2 GPa) compared with that (~1 GPa) in the mid-oceanic ridge basalt (MORB) composition in a high-temperature anomalous environment, such as under hot spots (Hirose et al., 1999; Hirose, 2002; Jenkins et al., 2016). In a subduction setting, the majorite in peridotite will first change to akimotoite (ilmenite) and then to bridgmanite. This scenario is inconsistent with our present obser-

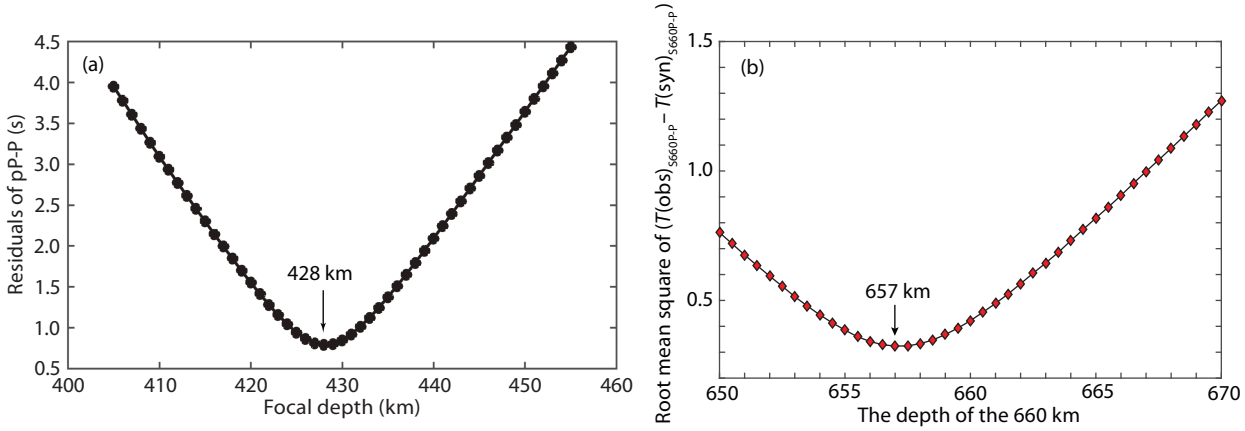

Figure 7. (a) The event used in this study occurring at a focal depth of 428 km, which best fits the pP-P differential travel times. (b) The S-to-P conversion occurring at a 657-km depth, which best fits the S660P-P differential travel times.

Table 1. Information for ten stations recorded S660P waveforms for calculating amplitude ratio of S660P versus S.

Station code	Lat. (°)	Lon. (°)
BPAW	64.099	−150.987
BWN	64.173	−149.299
CAST	63.418	−152.084
CHUM	63.882	−152.315
KNK	61.413	−148.458
MLY	65.030	−150.744
PPLA	62.896	−152.189
PWL	60.858	−148.333
RC01	61.088	−149.739
TRF	63.450	−150.289

vation. If this transition does take control, it is believed to produce two discontinuities (majorite to ilmenite and ilmenite to bridgmanite) in addition to the 660-km interface by the olivine phase change. Moreover, the phase transformation of majorite–ilmenite–bridgmanite is thought to occur at a shallower level above the 660-km depth (Hirose, 2002). As a result, the present scenario cannot be explained by the transformation of majorite–bridgmanite to peridotite. Therefore, when considering phase changes in the MORB, it is of great importance to explain the mantle discontinuities beneath subduction zones.

Emerging evidence has shown the existence of a low-velocity layer (LVL) in the uppermost lower mantle caused by dehydration-related melting (e.g., Schmandt et al., 2014; Liu Z et al., 2016). To examine whether an LVL model could explain the observed signal, we constructed a series of models to fit the data (Figure 13). Even though the best LVL model largely explained the data, the cross-correlation coefficient was still lower than that given by the positive gradient discontinuity model (Figure 12). Our analyses further ruled out the negative gradient discontinuity model (Figure 14) and pyrope model (Figure 15) given by Wang WZ and Wu ZQ (2018). Pyrope decomposition can result in V_P, V_S, and density jumps of 12.4%, 20%, and 9.8%, respectively, as suggested by their calculation based on density-functional theory. Because we had no prior constraints on the fraction of pyrope in the uppermost mantle, we then tried a series of fractions to compare with the data. The fraction that was best able to explain the observations was 12%, leading to a moderate waveform cross-correlation

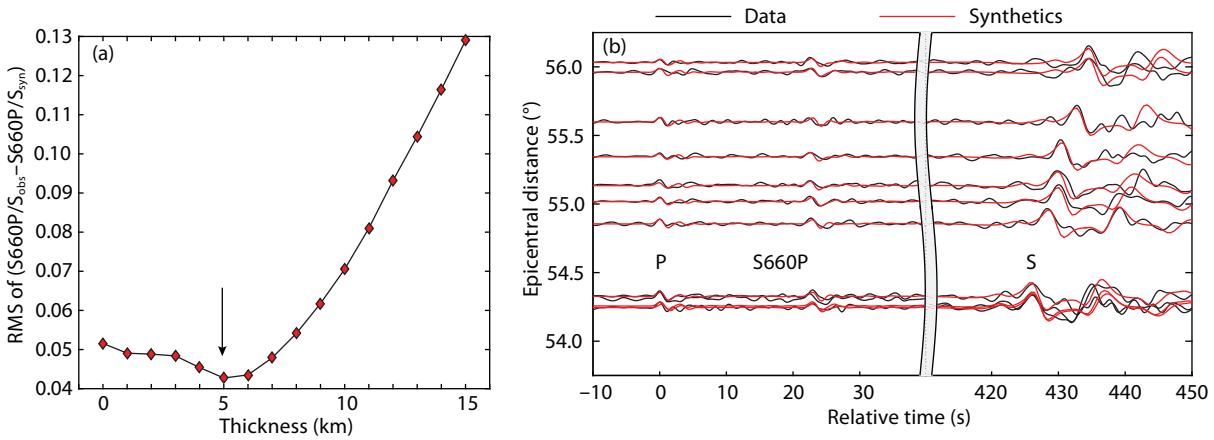

Figure 8. (a) The transition thickness of the 660-km discontinuity is ~5 km, which best explains the amplitude ratio of S660P versus S. (b) Comparisons of waveforms between the data and the synthetics according to the preferred model shows good agreement between them.

coefficient (0.77), which is still less than that (0.97) given by the MORB model.

Subducted oceanic crust is mainly composed of MORB, which undergoes a phase transformation to bridgmanite at ~720-km depth (the transition pressure also depends on the Al_2O_3 content of the MORB) with a small positive Clapeyron slope (Hirose et al., 1999). More importantly, the transitional width of 20 km in our model (equivalent to a 1-GPa interval) is consistent with the experimental prediction of Hirose et al. (1999). Hence, the 720-km discontinuity detected in this study was most likely caused by the transformation of MORB to a bridgmanite lithology.

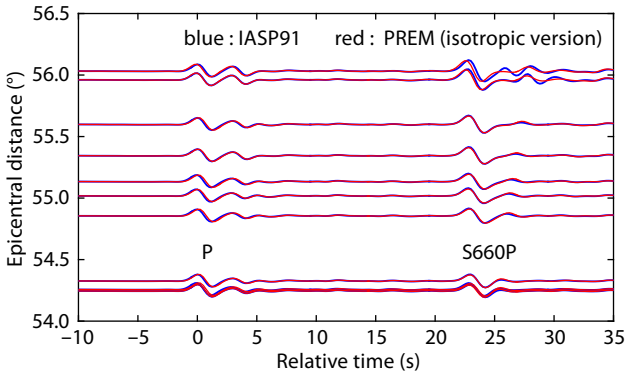

Figure 9. Comparisons in synthetic S660P waveforms according to the impedance contrast across the 660-km depth given by the IASP91 and PREM models.

Again, the 720-km discontinuity seen here ranged precisely from depths of 725 to 745 km. A similar phenomenon of double 660-km discontinuities has been observed in the receiver functions beneath northeast China (Ai YS et al., 2003). Even more important is that the coda after the 660-km phase also occurred around a depth of 720–730 km. Furthermore, discontinuities around 720 km were detected beneath southern California by analyzing Pds (P converted to S at depth d) and PPds (similar to Pds, but for an incoming PP phase). A discontinuity at a depth of around 730–740 km has also been noted beneath the areas of Tonga (Zang SX et al., 2006) and Izu–Bonin (Zhou YZ et al., 2012). The 720-km discontinuity observed in those areas could also have been due to a phase change of majorite in the MORB. In reality, multiple discontinuities below the 660-km depth (i.e., more than one discontinuity) seen in the regional and global data at the top of the lower mantle (e.g., Simmons and Gurrola, 2000; Deuss et al., 2006; Zang SX et al., 2006; Zhou YZ et al., 2012; Lessing et al., 2014) can be explained by the transformation of MORB with various Al_2O_3 contents (Hirose et al., 1999). The precise Al_2O_3 contents require new

Table 2. Information for four stations recorded SdP waveforms for calculating amplitude ratio of S660P versus PcP.

Station code	Lat. (°)	Lon. (°)
BPAW	64.099	−150.987
MLY	65.030	−150.744
NEA	64.592	−149.071
PPLA	62.896	−152.189

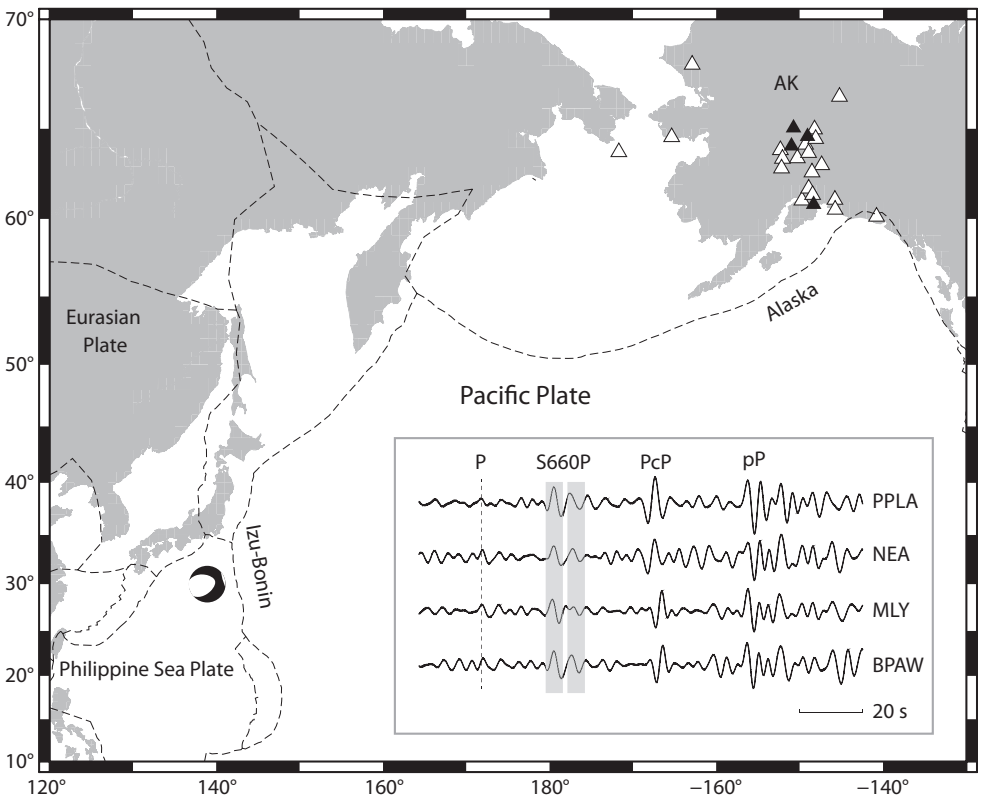

Figure 10. The same as Figure 1, but the inset shows waveforms recorded at four stations (PPLA, NEA, MLY, BPAW), as indicated by the solid triangles. The gray-shaded region highlights the double signals arriving in the P-coda.

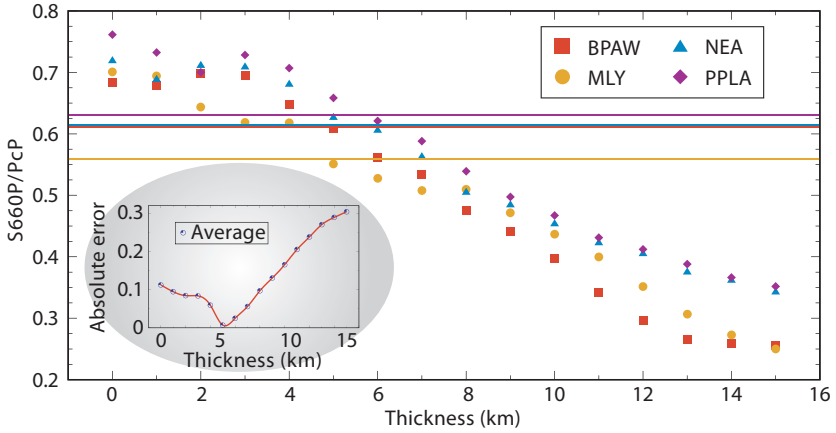

Figure 11. Comparisons in terms of amplitude ratio of S660P versus PcP between the data (colored lines) recorded at four stations and a series of models (four colored symbols) constructed by varying the transitional thickness of the S-to-P conversion at the 660-km depth by an increment of 1 km and using the same impedance contrast as for the IASP91 model. The bottom left inset indicates that the thickness of the 660-km discontinuity is ~5 km, which best explains the data.

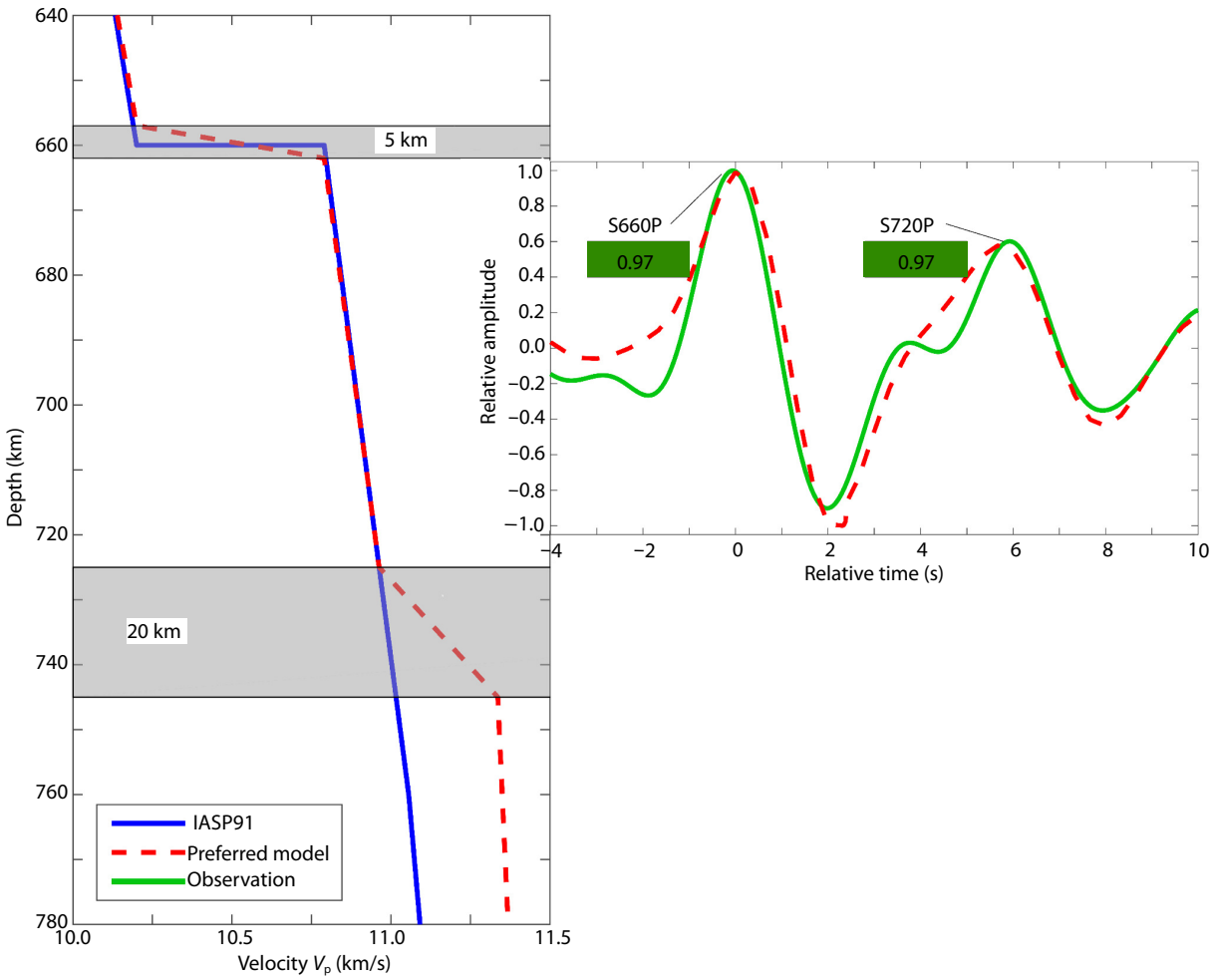

Figure 12. Left: A preferred shear-wave velocity profile (dashed red line) comprising a discontinuity below 660-km depth with a transition thickness of 20 km, generated by modifying the IASP91 model (blue line). Right: comparison of the data (slant-stacked waveform, green line) and a synthetic waveform (dashed red line). The waveform cross-correlation coefficients for both phases are marked.

knowledge obtained from future mineral physics experiments. In addition, the uppermost lower mantle is a layer in which subducted oceanic crust could be trapped, which may explain in part the deeper discontinuities, particularly at a depth of ~1,000 km (e.g., Yang ZT and He XB, 2015; He XB and Zheng YX, 2018). Caution must be exercised when interpreting double signals in terms of

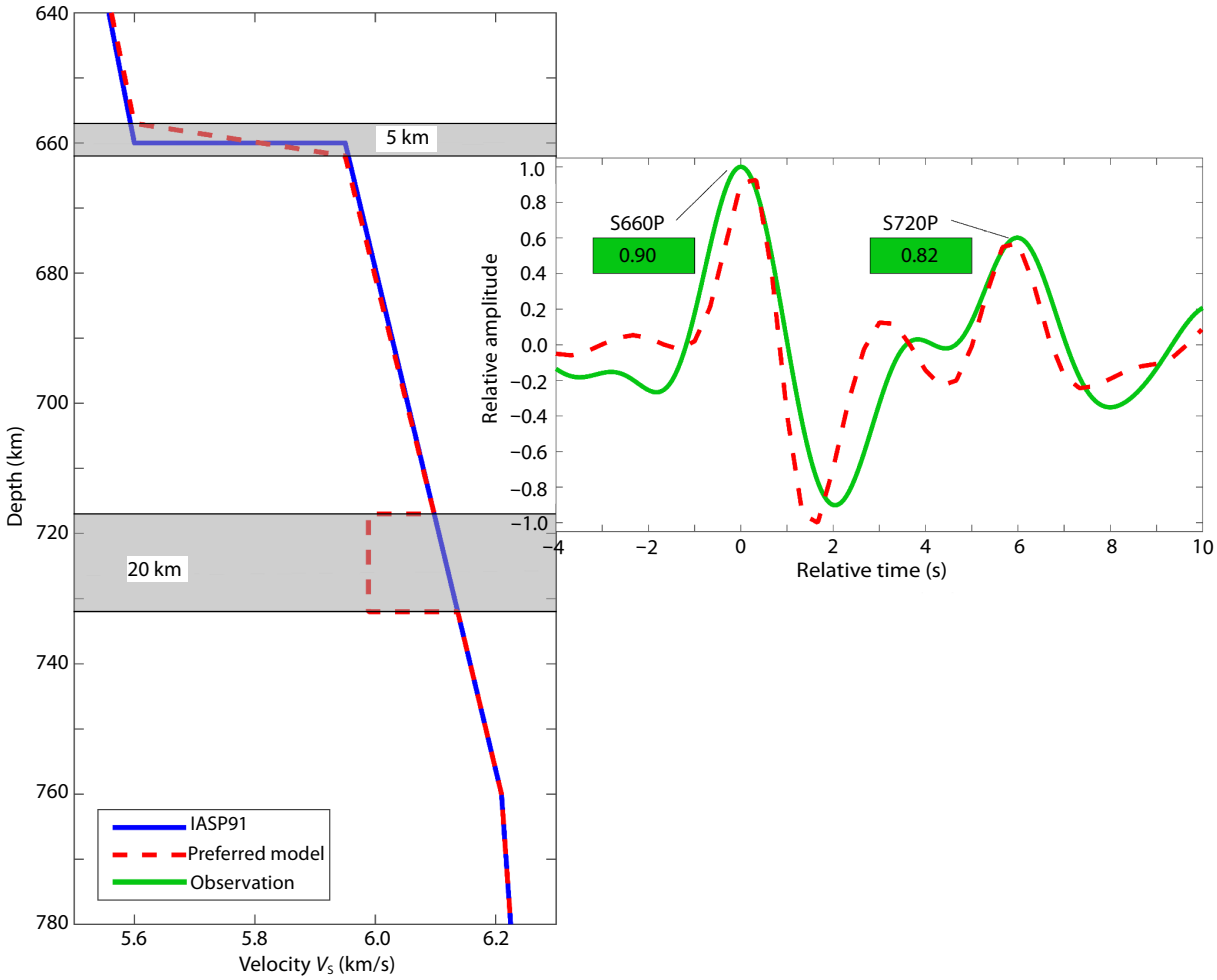

Figure 13. Left: a velocity profile comprising a low-velocity-layer (LVL) with V_S reduction by −1.5%, generated by modifying the IASP91 model (Kennett and Engdahl, 1991). Right: comparison of the data (slant-stacked waveform) and synthetic, and the waveform cross-correlation coefficients for both phases are marked.

complex mineralogical transitions because mantle heterogeneity subparallel to the great-circle path can occasionally produce artifacts (Zheng Z. and Romanowicz, 2012). Therefore, careful analyses of seismic signals from a wide range of azimuths and distances are important to avoid misinterpretations. Hence, a future study using data collected from stations with different azimuths would place tight constraints on the structures below the source in Izu–Bonin.

3.3 Uncertainty Analyses

We acknowledge that, because of the limited number of models evaluated to find suitable models, error has not been reported for each model. Although we were unable to quantitatively assess the uncertainty of the results, here we discuss possible factors that might result in error in the results. The first is the focal depth. To minimize uncertainty introduced by the focal depth, we used pP-P differential travel times to refine the depth. In addition, the depths of S-to-P conversions were constrained by analyzing differential travel times of S660P versus P and S660P versus S720P, which further reduced the uncertainty. The second is the velocity model. Here we used a one-dimensional velocity model given by the IASP91 model to constrain the S-to-P conversion depths, which somehow deviated from a true three-dimensional model, possibly leading to some uncertainty. Again, the use of differential travel times further helped reduce error introduced by the uncertainty in the velocity model. Only the velocity perturbations at depths ranging from the focal event to the S-to-P conversion pointed at the 660-km discontinuity, which could be ~130 km or less, likely leading to a minor uncertainty in the result. The third is the dipping interface of the 660-km discontinuity. It is true that a certain topography can occur at the interface because of thermal or chemical anomalies, or both (e.g., Wu WB et al., 2019), which can result in an unstable stacking of waveforms. However, the area defined by the S-to-P conversions at the 660-km depth (Figure 6) was, in fact, even smaller than the Fresnel zone defined by the S660P wave, and its radius was ~60 km at this depth. Consequently, the dipping effects were likely negligible.

We have discussed that the source radiation pattern had no apparent effects on the constrained sharpness, but the constrained transition thickness depended on the impedance contrast across the discontinuities. Note that the good-quality data presented in this study will still be useful to re-evaluate the sharpness if a different impedance contrast emerges in the future. We used teleseis-

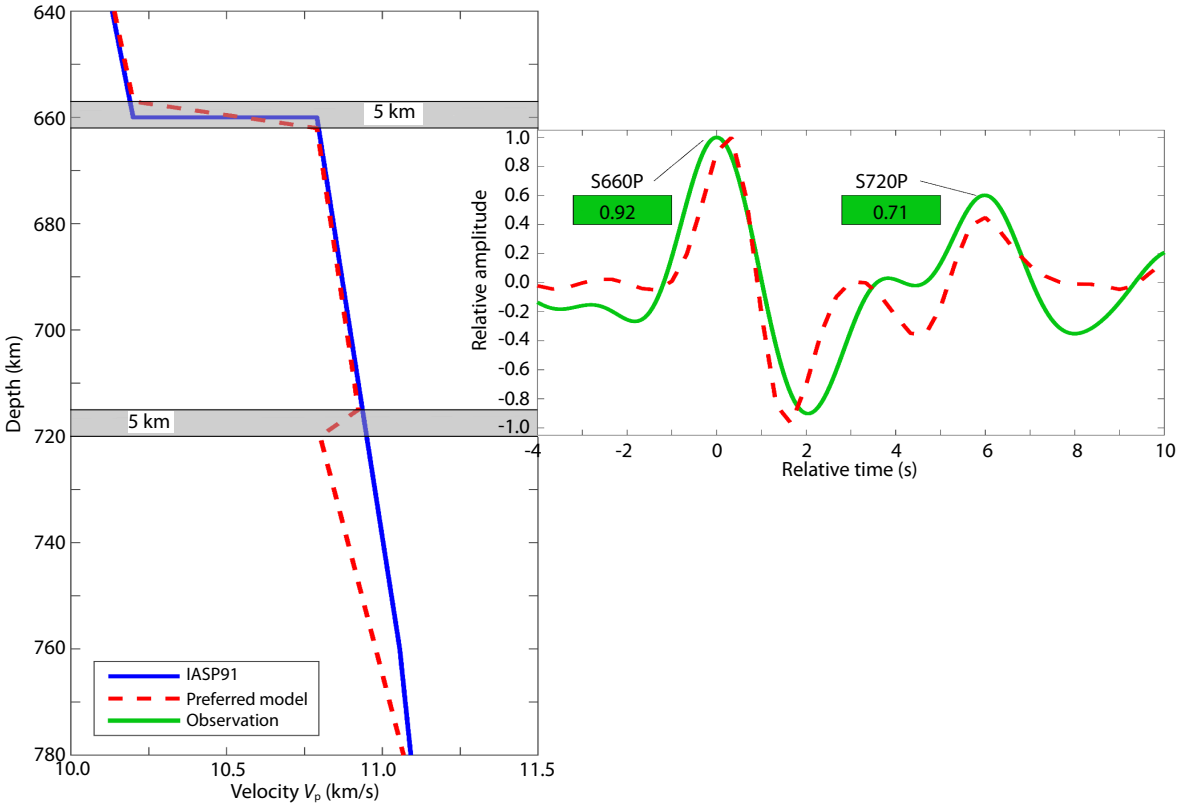

Figure 14. The same plot as shown in Figure 13, except here comprising a negative gradient.

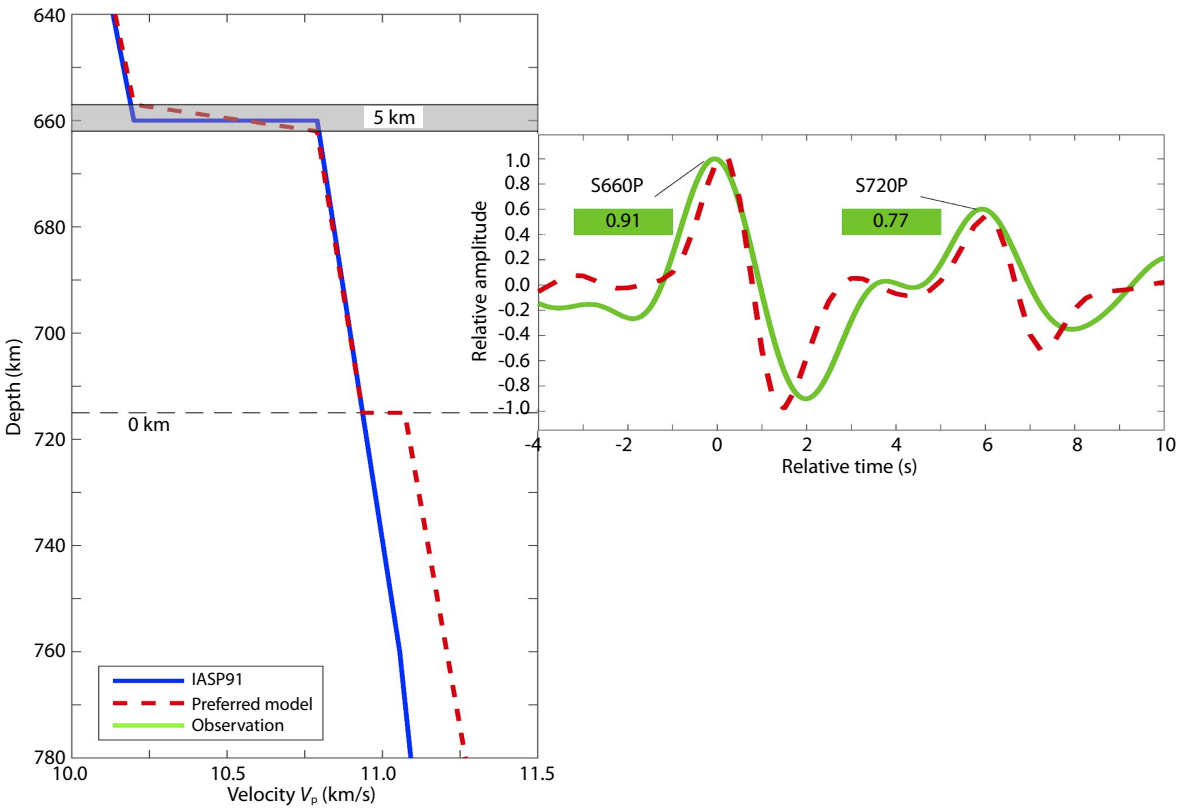

Figure 15. The same plot as shown in Figure 13, except here comprising the pyrope model (Wang WZ and Wu ZQ, 2018), in which the impedance contrast is calculated according to a fraction of 12% of pyrope in the deep mantle, which leads to the largest waveform cross-correlation coefficient (0.77) among various fractions.

mic data with frequencies ranging from 0.05 to 0.5 Hz in this study to constrain the sharpness. Whether sharpness of a frequency-dependent nature exists will not be fully understood until other seismic phases, such as precursors to PKPPKP with higher frequencies, are used for comparisons in the future. An early study on PKPPKP precursors (0.8–2.0 s) suggested the transition thickness as being 4 km or less (Benz and Vidale, 1993); when compared it with our results, no notable frequency-depedent signature is suggested. In addition, the number of observable S720P phases was less than that of S660P, suggesting that the 720-km discontinuity is not ubiquitous but sporadic and that its occurrence relies strongly on the presence of MORB materials, given that the oceanic crust is segregated in the uppermost lower mantle, particularly beneath subduction zones.

4. Conclusions

We observed double discontinuities at depths of ~660 and ~720 km beneath the Izu–Bonin subduction zone by using S-to-P conversions on the source side. The 660-km discontinuity with a transitional thickness of ~5 km was attributed to the phase transition from ringwoodite to bridgmanite and magnesiowüstite, whereas the 720-km discontinuity with a transitional thickness of ~20 km was most likely due to the phase transition of MORB to bridgmanite. Our observations are consistent with predictions from mineral physics experiments.

Acknowledgments

We are grateful for the thoughtful and constructive comments provided by two anonymous reviewers and the editor (Dr. Wei Leng). We also thank Jinfeng Hu for his contributions to this work at an early stage. Seismic data from the USArray network were accessed via the Data Management Center (DMC) of the Incorporated Research Institutions for Seismology (IRIS). Some figures were prepared using Generic Mapping Tools (GMT; Wessel and Smith, 1999) and GNUPLOT. This work was funded by the National Natural Science Foundation of China (grants nos. 91428309 and 41761134051).

References

Ai, Y. S., Zheng, T. Y., Xu, W. W., He, Y. M., and Dong, D. (2003). A complex 660 km discontinuity beneath northeast China. *Earth Planet. Sci. Lett.*, *212*(1-2), 63–71. https://doi.org/10.1016/S0012-821X(03)00266-8

Benz, H. M., and Vidale, J. E. (1993). Sharpness of upper-mantle discontinuities determined from high-frequency reflections. *Nature*, *365*(6442), 147–150. https://doi.org/10.1038/365147a0

Castle, J. C., and Creager, K. C. (2000). Local sharpness and shear wave speed jump across the 660-km discontinuity. *J. Geophys. Res. Solid Earth*, *105*(B3), 6191–6200. https://doi.org/10.1029/1999JB900424

Crotwell, H. P., Owens, T. J., and Ritsema, J. (1999). The TauP toolkit: flexible seismic travel-time and ray-path utilities. *Seismol. Res. Lett.*, *70*(2), 154–160. https://doi.org/10.1785/gssrl.70.2.154

Cui, Q. H., Li, W. L., Li, G. H., Ma, M. N., Guan, X. Y., and Zhou, Y. Z. (2018). Seismic detection of the X-discontinuity beneath the Ryukyu subduction zone from the SdP conversion phase. *Earth Planet. Phys.*, *2*(3), 208–219. https://doi.org/10.26464/epp2018020

Deuss, A., Redfern, S. A. T., Chambers, K., and Woodhouse, J. H. (2006). The nature of the 660-Kilometer discontinuity in Earth's mantle from global seismic observations of *PP* precursors. *Science*, *311*(5758), 198–201. https://doi.org/10.1126/science.1120020

Dziewonski, A. M., and Anderson, D. L. (1981). Preliminary reference Earth model. *Phys. Earth Planet. Inter.*, *25*(4), 297–356. https://doi.org/10.1016/0031-9201(81)90046-7

French, S. W., and Romanowicz, B. (2015). Broad plumes rooted at the base of the Earth's mantle beneath major hotspots. *Nature*, *525*(7567), 95–99. https://doi.org/10.1038/nature14876

Fukao, Y., and Obayashi, M. (2013). Subducted slabs stagnant above, penetrating through, and trapped below the 660 km discontinuity. *J. Geophys. Res. Solid Earth*, *118*(11), 5920–5938. https://doi.org/10.1002/2013JB010466

He, X. B., and Zheng, Y. X. (2018). S-to-P conversions from mid-mantle slow scatterers in slab regions: observations of deep/stagnated oceanic crust?. *Pure Appl. Geophys.*, *175*(6), 2045–2055. https://doi.org/10.1007/s00024-017-1763-z

Hirose, H. (2002). Phase transitions in pyrolitic mantle around 670-km depth: Implications for upwelling of plumes from the lower mantle. *J. Geophys. Res. Solid Earth*, *107*(B4), ECV 3-1–ECV 3-13. https://doi.org/10.1029/2001JB000597

Hirose, K., Fei, Y. W., Ma, Y. Z., and Mao, H. K. (1999). The fate of subducted basaltic crust in the Earth's lower mantle. *Nature*, *397*(6714), 53–56. https://doi.org/10.1038/16225

Hu, J. F., and He, X. B. (2019). Seismic evidence for a paleoslab in the D" layer residing adjacent to the southeastern edge of the perm anomaly. *Geochem. Geophys. Geosyst.*, *20*(4), 2040–2052. https://doi.org/10.1029/2019GC008195

Huang, J. P., Niu, F. L., Gordon, R. G., and Cui, C. (2015). Accurate focal depth determination of oceanic earthquakes using water-column reverberation and some implications for the shrinking plate hypothesis. *Earth Planet. Sci. Lett.*, *432*, 133–141. https://doi.org/10.1016/j.epsl.2015.10.001

Ishii, T., Huang, R., Myhill, R., Fei, H. Z., Koemets, I., Liu, Z. D., Maeda, F., Yuan, L., Wang, L., … Katsura, T. (2019). Sharp 660-km discontinuity controlled by extremely narrow binary post-spinel transition. *Nat. Geosci.*, *12*(10), 869–872. https://doi.org/10.1038/s41561-019-0452-1

Ito, E., and Takahashi, E. (1989). Postspinel transformations in the system Mg_2SiO_4-Fe_2SiO_4 and some geophysical implications. *J. Geophys. Res. Solid Earth*, *94*(B8), 10637–10646. https://doi.org/10.1029/JB094iB08p10637

Jenkins, J., Cottaar, S., White, R. S., and Deuss, A. (2016). Depressed mantle discontinuities beneath Iceland: Evidence of a garnet controlled 660 km discontinuity?. *Earth Planet. Sci. Lett.*, *433*, 159–168. https://doi.org/10.1016/j.epsl.2015.10.053

Kennett, B. L. N., and Engdahl, E. R. (1991). Traveltimes for global earthquake location and phase identification. *Geophys. J. Int.*, *105*(2), 429–465. https://doi.org/10.1111/j.1365-246X.1991.tb06724.x

Lawrence, J. F., and Shearer, P. M. (2006). A global study of transition zone thickness using receiver functions. *J. Geophys. Res. Solid Earth*, *111*(B6), B06307. https://doi.org/10.1029/2005JB003973

Lessing, S., Thomas, C., Rost, S., Cobden, L., and Dobson, D. P. (2014). Mantle transition zone structure beneath India and Western China from migration of *PP* and *SS* precursors. *Geophys. J. Int.*, *197*(1), 396–413. https://doi.org/10.1093/gji/ggt511

Li, J., Wang, X., Wang, X. J., and Yuen, D. A. (2013). P and SH velocity structure in the upper mantle beneath Northeast China: Evidence for a stagnant slab in hydrous mantle transition zone. *Earth Planet. Sci. Lett.*, *367*, 71–81. https://doi.org/10.1016/j.epsl.2013.02.026

Li, J., and Yuen, D. A. (2014). Mid-mantle heterogeneities associated with Izanagi plate: Implications for regional mantle viscosity. *Earth Planet. Sci. Lett.*, *385*, 137–144. https://doi.org/10.1016/j.epsl.2013.10.042

Liu, Z., Park, J., and Karato, S. I. (2016). Seismological detection of low-velocity anomalies surrounding the mantle transition zone in Japan subduction zone. *Geophys. Res. Lett.*, *43*(6), 2480–2487. https://doi.org/10.1002/2015GL067097

Niu, F. L. (2014). Distinct compositional thin layers at mid-mantle depths beneath northeast China revealed by the USArray. *Earth Planet. Sci. Lett.*, *402*, 305–312. https://doi.org/10.1016/j.epsl.2013.02.015

Petersen, N., Vinnik, L., Kosarev, G., Kind, R., Oreshin, S., and Stammler, K. (1993). Sharpness of the mantle discontinuities. *Geophys. Res. Lett.*, *20*(9), 859–862. https://doi.org/10.1029/93GL00684

Ringwood, A. E. (1975). *Composition and Petrology of the Earth's Mantle*. New York: McGraw-Hill.

Rost, S., and Thomas, C. (2002). Array seismology: methods and applications. *Rev. Geophys.*, *40*(3), 2-1–2-27. https://doi.org/10.1029/2000RG000100

Schmandt, B., Jacobsen, S. D., Becker, T. W., Liu, Z. X., and Dueker, K. G. (2014). Dehydration melting at the top of the lower mantle. *Science*, *344*(6189), 1265–1268. https://doi.org/10.1126/science.1253358

Schultz, R., and Gu, Y. J. (2013). Multiresolution imaging of mantle reflectivity structure using SS and PP precursors. *Geophys. J. Int.*, *195*(1), 668–683. https://doi.org/10.1093/gji/ggt266

Shearer, P. M., and Masters, T. G. (1992). Global mapping of topography on the 660-km discontinuity. *Nature*, *355*(6363), 791–796. https://doi.org/10.1038/355791a0

Shearer, P. M. (2000). Upper mantle seismic discontinuities. In S. I. Karato, et al. (Eds.), *Earth's Deep Interior: Mineral Physics and Tomography from the Atomic to the Global Scale* (pp. 115-131). Washington: AGU. https://doi.org/10.1029/GM117p0115

Simmons, N. A., and Gurrola, H. (2000). Multiple seismic discontinuities near the base of the transition zone in the Earth's mantle. *Nature*, *405*(6786), 559–562. https://doi.org/10.1038/35014589

Tibi, R., and Wiens, D. A. (2005). Detailed structure and sharpness of upper mantle discontinuities in the Tonga subduction zone from regional broadband arrays. *J. Geophys. Res. Solid Earth*, *110*(B6), B06313. https://doi.org/10.1029/2004JB003433

Tibi, R., Wiens, D. A., Shiobara, H., Sugioka, H., and Yuan, X. H. (2007). Double seismic discontinuities at the base of the mantle transition zone near the Mariana slab. *Geophys. Res. Lett.*, *34*(16), L16316. https://doi.org/10.1029/2007GL030527

Vacher, P., Mocquet, A., and Sotin, C. (1998). Computation of seismic profiles from mineral physics: the importance of the non-olivine components for explaining the 660 km depth discontinuity. *Phys. Earth Planet. Inter.*, *106*(3-4), 275–298. https://doi.org/10.1016/S0031-9201(98)00076-4

Vitos, L., Magyari-Köpe, B., Ahuja, R., Kollár, J., Grimvall, G., and Johansson, B. (2006). Phase transformations between garnet and perovskite phases in the Earth's mantle: a theoretical study. *Phys. Earth Planet. Inter.*, *156*(1-2), 108–116. https://doi.org/10.1016/j.pepi.2006.02.004

Wang, B. S., and Niu, F. L. (2010). A broad 660 km discontinuity beneath northeast China revealed by dense regional seismic networks in China. *J. Geophys. Res. Solid Earth*, *115*(B6), B06308. https://doi.org/10.1029/2009JB006608

Wang, R. J. (1999). A simple orthonormalization method for stable and efficient computation of Green's functions. *Bull. Seismol. Soc. Am.*, *89*(3), 733–741.

Wang, W. Z., and Wu, Z. Q. (2018). Elasticity of corundum at high pressures and temperatures: Implications for pyrope decomposition and Al-content effect on elastic properties of bridgmanite. *J. Geophys. Res. Solid Earth*, *123*(2), 1201–1216. https://doi.org/10.1002/2017JB015088

Wessel, P., and Smith, W. H. F. (1999). Free software helps map and display data. *Eos*, *72*(41), 441–446. https://doi.org/10.1029/90EO00319

Wu, W. B., Ni, S. D., and Irving, J. C. E. (2019). Inferring Earth's discontinuous chemical layering from the 660-kilometer boundary topography. *Science*, *363*(6428), 736–740. https://doi.org/10.1126/science.aav0822

Yamazaki, A., and Hirahara, K. (1994). The thickness of upper mantle discontinuities, as inferred from short-period J-Array data. *Geophys. Res. Lett.*, *21*(17), 1811–1814. https://doi.org/10.1029/94GL01418

Yang, Z. T., and He, X. B. (2015). Oceanic crust in the mid-mantle beneath west-central Pacific subduction zones: evidence from *S* to *P* converted waveforms. *Geophys. J. Int.*, *203*(1), 541–547. https://doi.org/10.1093/gji/ggv314

Zang, S. X., Zhou, Y. Z., Ning, J. Y., and Wei, R. Q. (2006). Multiple discontinuities near 660 km beneath Tonga area. *Geophys. Res. Lett.*, *33*(20), L20312. https://doi.org/10.1029/2006GL027262

Zhang, M., Sun, D. Y., Wang, Y., and Wu, Z. Q. (2019). Fine structure of the 660-km discontinuity beneath southeastern China. *Geophys. Res. Lett.*, *46*(13), 7304–7314. https://doi.org/10.1029/2019GL082639

Zheng, Z., and Romanowicz, B. (2012). Do double "SS precursors" mean double discontinuities?. *Geophys. J. Int.*, *191*(3), 1361–1373. https://doi.org/10.1111/j.1365-246X.2012.05683.x

Zhou, Y. Z., Yu, X. W., Yang, H., and Zang, S. X. (2012). Multiplicity of the 660-km discontinuity beneath the Izu-Bonin area. *Phys. Earth Planet. Inter.*, *198-199*, 51–60. https://doi.org/10.1016/j.pepi.2012.03.003